NANOPHOTONICS

Cavity-mediated electron-photon pairs

Armin Feist[1,2]†, Guanhao Huang[3,4]†, Germaine Arend[1,2]†, Yujia Yang[3,4]†, Jan-Wilke Henke[1,2], Arslan Sajid Raja[3,4], F. Jasmin Kappert[1,2], Rui Ning Wang[3,4], Hugo Lourenço-Martins[1,2], Zheru Qiu[3,4], Junqiu Liu[3,4], Ofer Kfir[1,2], Tobias J. Kippenberg[3,4]*, Claus Ropers[1,2]*

Quantum information, communication, and sensing rely on the generation and control of quantum correlations in complementary degrees of freedom. Free electrons coupled to photonics promise novel hybrid quantum technologies, although single-particle correlations and entanglement have yet to be shown. In this work, we demonstrate the preparation of electron-photon pair states using the phase-matched interaction of free electrons with the evanescent vacuum field of a photonic chip–based optical microresonator. Spontaneous inelastic scattering produces intracavity photons coincident with energy-shifted electrons, which we employ for noise-suppressed optical mode imaging. This parametric pair-state preparation will underpin the future development of free-electron quantum optics, providing a route to quantum-enhanced imaging, electron-photon entanglement, and heralded single-electron and Fock-state photon sources.

Optical parametric processes generate quantum correlations of photons without changing the state of the optical medium involved. Entangled photons from parametric down-conversion (*1*) are an essential resource for heralded single-photon sources, quantum communication, and quantum teleportation (*2*). Spatially separated entanglement afforded by such "twin beam" pairs was extended to various physical contexts, with examples in atomic beams (*3*), electron spins (*4*), and photon-phonon correlations in micromechanical systems (*5*). Free-electron beams are an emerging target for quantum manipulation and sensing, promising quantum-enhanced imaging (*6*, *7*), spectroscopy (*8*–*10*), and excitation (*11*–*14*). A variety of technologies that bridge electron microscopy and photonics (*15*) are being established to join the most powerful probes in atomic-scale imaging and spectroscopy, respectively. Among these, stimulated near-field scattering offers mode-specific probing of optical properties, whereas spontaneous electron energy loss and cathodoluminescence access electronic transitions and the total photonic density of states (*15*). Structural design has been shown to allow for a tailoring of the spectral and spatial properties of electron-driven radiation (*16*, *17*). Harnessing quantum optics approaches, measurements of photon statistics are used to reveal single quantum emitters (*18*) or photon bunching (*19*, *20*). Theoretical work predicted single-photon cathodoluminescence into a waveguide (*21*), and recent experiments studied the electron-induced excitation of whispering gallery modes (*22*, *23*) and optical fibers (*24*). However, impeded by a lack of mode-specific and sufficiently strong coupling, correlations between single electrons and well-defined photonic states have remained elusive. In this study, we use spontaneous inelastic scattering via the evanescent field of a high–quality factor (Q) photonic chip–based optical microresonator to generate free-electron cavity-photon pair states. We characterize the dual-particle heralding efficiencies and demonstrate coincidence imaging of the cavity mode with a substantial background suppression.

The interaction of electron beams with cavities and resonant structures represents a universal scheme for generating electromagnetic radiation. In the quantum optical description, the inelastic scattering can be modeled as a coupling of free electrons to optical vacuum fields (*8*). Scattering with the evanescent field of the optical microresonator, an electron at energy E, generates intracavity photons at frequencies ω in an energy-conserving manner (Fig. 1A), described by the scattering matrix $\hat{S} = \exp\left(g_{\mathrm{qu}}\hat{a}^{\dagger}\hat{b} - h.c.\right)$. Here, $\hat{a}^{\dagger}$ is the creation operator of the optical mode, g_{qu} is the vacuum coupling strength (*25*, *26*), and *h.c.* is the Hermitian conjugate. The ladder operator $\hat{b}$ reduces the energy of an electron by that of one photon. The interaction induces entanglement between the electron energy and the cavity population and results in the state

$$\left|\psi_{\mathrm{e}}, \psi_{\mathrm{ph}}\right\rangle = \sum_{n=0}^{\infty} c_n \left|E - n\hbar\omega\right\rangle \left|n\right\rangle \qquad (1)$$

(ψ_{e}, electron state; ψ_{ph}, photonic state; $\hbar$, reduced Planck's constant) with the coefficients $c_n = \exp\left(-\frac{|g_{\mathrm{qu}}|^2}{2}\right)\frac{g_{\mathrm{qu}}^n}{\sqrt{n!}}$ corresponding to Poissonian scattering probabilities (*25*). For a weak vacuum coupling strength $|g_{\mathrm{qu}}| \ll 1$, the state is dominated by the zero- and one-photon contributions

$$\left|\psi_{\mathrm{e}}, \psi_{\mathrm{ph}}\right\rangle \propto \left|E\right\rangle\left|0\right\rangle + g_{\mathrm{qu}}\left|E - \hbar\omega\right\rangle\left|1\right\rangle + \mathcal{O}\left(g_{\mathrm{qu}}^2\right) \qquad (2)$$

where $\mathcal{O}$ is order of approximation. Our measurements are designed to probe this state by detecting single photons in coincidence with inelastically scattered electrons by the energy of one photon. In the experiment, the continuous electron beam of a transmission electron microscope [120-keV beam energy, 25-nm focal diameter; see (*27*) section S1.3] traverses a photonic chip–based microresonator (Fig. 1C) and interacts with the vacuum fields to populate empty cavity modes.

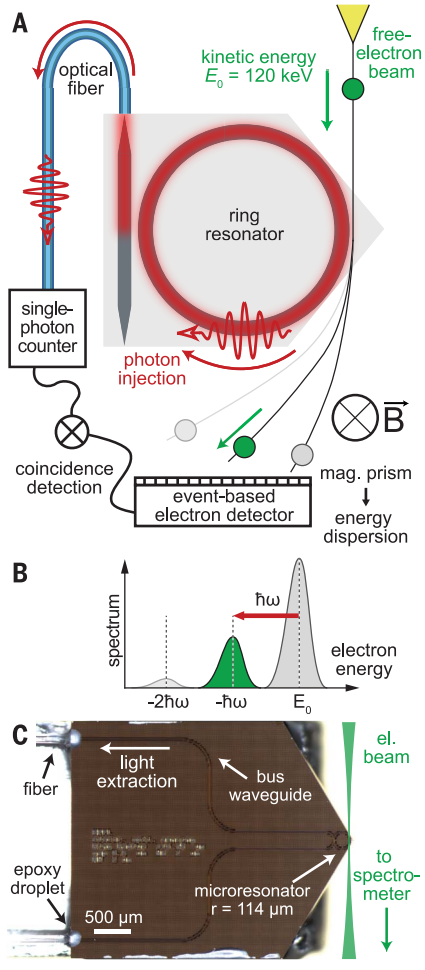

Fig. 1. Coincidence detection of electron-photon pairs generated at a photonic chip. (**A**) High-energy electrons traverse a fiber-coupled Si_3N_4 microring resonator, generating intracavity photons. Single photons and inelastically scattered electrons are detected in coincidence. $\vec{B}$, magnetic field. (**B**) Electron spectrum after interaction. (**C**) Optical microscope image of the photonic chip with a sketch of the passing electron beam. r, microresonator radius.

[1]Max Planck Institute for Multidisciplinary Sciences, D-37077 Göttingen, Germany. [2]4th Physical Institute – Solids and Nanostructures, University of Göttingen, D-37077 Göttingen, Germany. [3]Institute of Physics, Swiss Federal Institute of Technology Lausanne (EPFL), CH-1015 Lausanne, Switzerland. [4]Center for Quantum Science and Engineering, Swiss Federal Institute of Technology Lausanne (EPFL), CH-1015 Lausanne, Switzerland.
*Corresponding author. Email: claus.ropers@mpinat.mpg.de (C.R.); tobias.kippenberg@epfl.ch (T.J.K.)
†These authors contributed equally to this work.

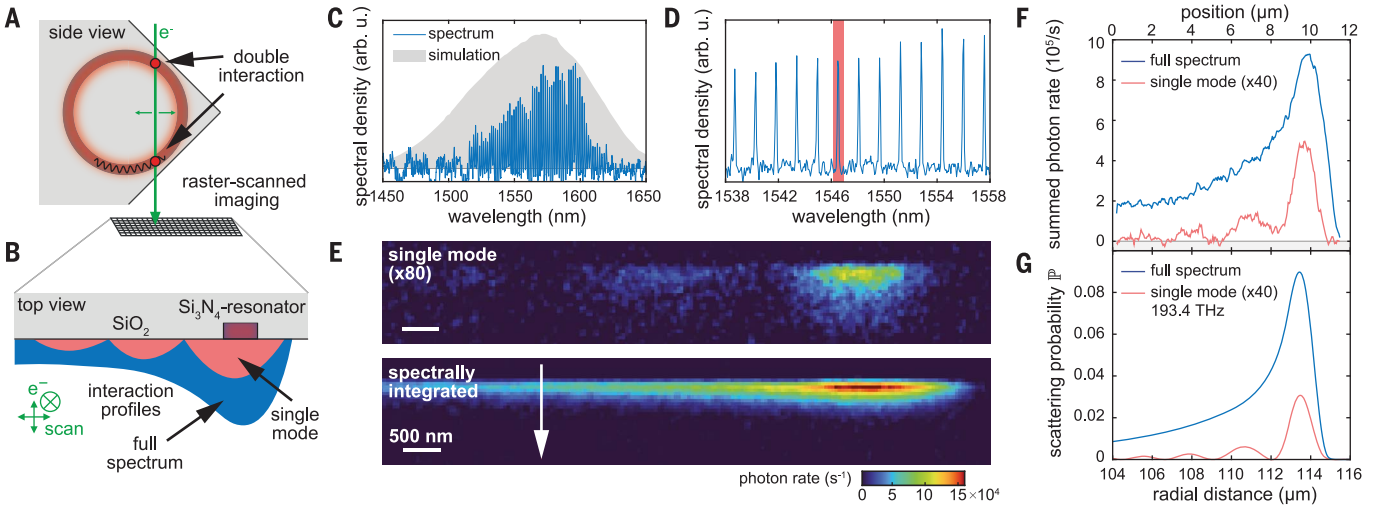

Fig. 2. Spatial and spectral mapping of intracavity photon generation. (**A** and **B**) Schematic of the measurement geometry. The electron beam (green) passes parallel to the chip surface (gray) and interacts twice (red dots) with the ring resonator (dark red). (**C**) Optical emission spectrum (blue; electron beam passes resonator tangentially) and simulated spectral envelope (gray). (**D**) Close-up view of the spectral mode comb and a selected single cavity mode (red). (**E**) Raster-scanned photon-generation maps [saturation corrected; see (*27*) S1.4] for the selected mode and the full spectrum [intensity patterns illustrated in (B) with red and blue]. (**F**) Signals from (E) integrated along the direction of the white arrow. (**G**) Simulation of the position-dependent electron scattering probability (50-nm distance).

The Si_3N_4 microresonator (*28*) is designed for low optical loss, efficient fiber coupling, and free-space near-field access [for optical characteristics, see (*27*) S1.2]. Enhancing the interaction by electron-light phase matching (*29*–*32*), we engineered the resonator cross section (2.1 μm by 650 nm) (*26*) for maximum photon generation probability per electron, which is predicted up to 10% around 0.8-eV photon energy (a wavelength of 1.55 μm).

Cavity photons generated in the clockwise propagating mode (Fig. 1A) are coupled out to a bus waveguide and are further guided by optical fibers to a single-photon avalanche diode (SPAD). The energy and arrival time of each electron is measured with an event-based detector behind a magnetic prism spectrometer (Fig. 1B), allowing for electron-photon coincidence experiments.

First, we spatially and spectrally map the electron-induced cavity excitation by placing the electron beam in proximity of the resonator (Fig. 2, A and B). Measured with an optical spectrometer, the overall spectral range of detected radiation spans from 1520 to 1620 nm, primarily limited by the bandwidth of electron-light phase matching and consistent with numerical simulations [Fig. 2C; see (*27*) S2.2]. The spectrum exhibits a comb-like structure (Fig. 2D) as a result of free-electron coupling to the microresonator modes a_μ [μ, mode index; see (*27*) S2.1 for a multimode description of the interaction]. The 1.58-nm spacing of the emission peaks matches the optically characterized quasi–transverse magnetic mode free-spectral range and confirms the predominant photon extraction from this mode family [see (*27*) S1.2].

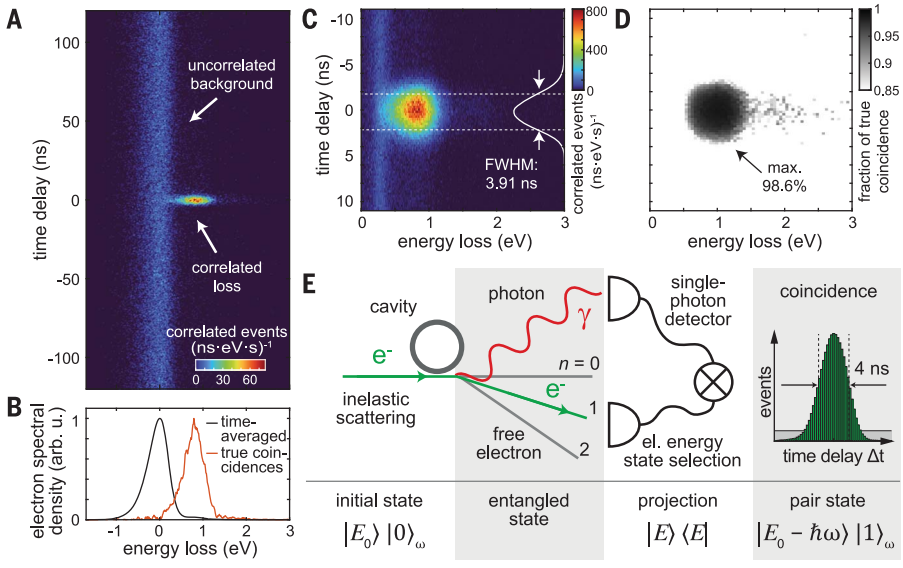

Fig. 3. Time- and energy-correlated electron-photon pairs. (**A**) Two-dimensional correlation histogram over the electron energy and relative photon timing (30-s integration, 0.65-pA electron current on detector) showing a strong coincidence peak. (**B**) Spectral distributions of the uncorrelated and correlated electrons (background subtracted). (**C** and **D**) Close-up view of correlation histogram (ZLP blocked, 60-s integration, 46-pA beam current at sample) with coincidence time trace (white) and fraction of true coincidences. FWHM, full width at half maximum. (**E**) Illustration of cavity-mediated inelastic electron-photon scattering and coincidence measurement.

Spatial characterization of the intracavity excitation is obtained by raster scanning of the electron beam (Fig. 2, A and B) and detection of emitted light with a SPAD. Figure 2E displays the obtained single-mode (top) and spectrally integrated (bottom) photon rates, which decay exponentially with distance from the structure, tracing the near-field mode profile in this spectral range. The strongest photon generation is observed for electrons passing the ring resonator tangentially, as expected for phase-matched electron-light interaction. Figure 2F shows the photon generation rates along the chip surface. The single-mode count rate shows a pronounced oscillation in the radial distance to the center of the ring resonator.

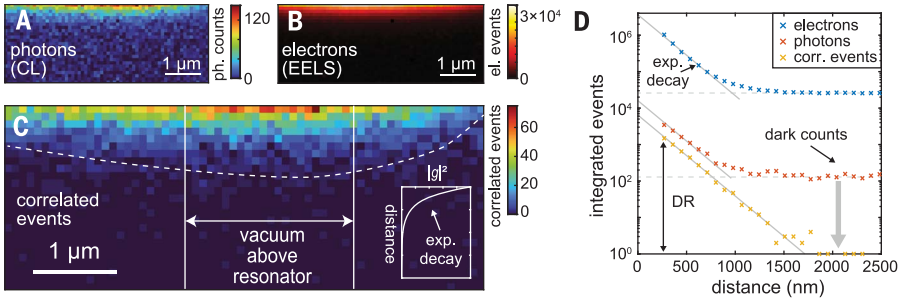

Fig. 4. Correlation-enhanced cavity mode imaging. Spatial distributions of (**A**) photons [cathodoluminescence (CL)], (**B**) loss-scattered electrons [electron energy-loss spectroscopy (EELS)], and (**C**) correlated events (30-ms integration per pixel, starting ~270 nm above the chip surface; see Fig. 2 for measurement geometry). The positions of the resonator and the mode envelope (solid and dashed lines, respectively, serve as a guide to the eye) are indicated. (Inset) Sketch of the cavity field decay into the vacuum (scattering probability $|g|^2$). The energy windows applied to (B) and (C) are optimized individually [see (*27*) S1.6]. (**D**) Logarithmic plot comparing the distance-dependent exponential mode decay from (A) to (C) (integrated in the area above the resonator, effectively 1-s acquisition per point). The lowest noise and highest dynamic range (DR) (more than three orders of magnitude) are observed for the time-correlated imaging.

This is caused by the interference between sequential interactions (Fig. 2A) of an electron with the cavity vacuum field (*33*), proving the conservation of mutual coherence in the scattering process. Similar Ramsey-type interference is also observed for an externally pumped ring resonator (*26*). Integrating the full mode spectrum of the cathodoluminescence averages out the oscillatory pattern, in agreement with numerical simulations (Fig. 2G). The total scattering probability is modeled as the sum $\mathbb{P} = \sum_{\mu} \left| g_{\mathrm{qu},\mu} \right|^2$ of the individual mode contributions $g_{\mathrm{qu},\mu}$ [see (*27*) S1.1 for details].

The spontaneous creation of photons by single electrons satisfies energy-momentum conservation, lowering the energy of an electron by $\hbar\omega$ and transferring the corresponding momentum to the cavity photon (*21*). We probe this correlated electron-photon pair state by coincidence measurements of both particles (Fig. 3). The electron beam is held fixed in the near field of the cavity at a distance of ~160 nm from the surface. At this position, we detect photons with a probability of 4.6×10^{-5} per electron passing the structure. Considering coupling and detection losses [see (*27*) S1.4], this corresponds to an intrinsic generation probability of ~2.5%.

The arrival time and kinetic energy of each electron is measured by event-based spectroscopy, using the stream of photon events recorded by the SPAD for time tagging [Fig. 1A and (*27*) S1.5 for details]. Figure 3A shows the energy- and time-dependent histogram of electron arrivals relative to the photon event closest in time. The two main features observed are a time-independent background of accidental coincidences around zero energy loss and an anticipated sharp correlation peak around 0.8-eV energy loss and 0-ns time delay. The spectrum of the correlated electrons (Fig. 3B, red) is downshifted by the energy of one photon with respect to the zero-loss peak (ZLP) (black). As a result of the narrow electron-light phase-matching bandwidth of ~50 meV, these spectral distributions are very similar in broadening and shape [~0.5-eV width; see (*27*) S1.6 for details].

We next insert a mechanical slit in the electron spectrometer (Fig. 3C) to reject electrons that were not scattered, allowing for higher total electron flux, and thus photon rates, without detector saturation. The background-corrected time profile (inset) shows the precise temporal structure of the correlated electron-photon pairs with a width of 3.91 ns. In principle, the temporal correlation trace should reproduce the cavity decay time, but it is not resolved in the present experiments [current device: ~0.5-ns lifetime for $Q \sim 5.5 \times 10^5$; see (*27*) S1.2].

By selecting loss-scattered electrons within a specific time window, we identify correlated events on a single-particle basis. The measurement of the electron energy for each event, in contrast to conventional optical spontaneous parametric down-conversion, presents a direct measure of the energy quanta n deposited in the optical cavity. The single-electron energy detection at the first energy loss sideband therefore represents an optical state projection from the entangled state (Eq. 1) onto the (nonclassical) single-photon intracavity Fock state (*13*, *21*, *25*). This general principle, illustrated in the schematic of Fig. 3E, enables interparticle heralding schemes for either electrons or photons. Notably, interactions with multiple electrons—relevant for studying electron-electron correlations—can be excluded owing to the multihit capability of the detector.

Such heralded particle sources are quantified in terms of the measured rates of electrons (R_{e}), photons (R_{p}), and correlated events (R_{pe}) and the Klyshko heralding efficiencies $\eta_{\mathrm{K}}^{i} = R_{\mathrm{pe}}/R_j$ ($i, j = \mathrm{e}, \mathrm{p}, i \neq j$), which describe the conditional probability of experimentally detecting a heralded particle [see (*27*) S1.6]. For the data shown in Fig. 3C, we measure $\eta_{\mathrm{K}}^{\mathrm{p}} \sim 0.11\%$ and $\eta_{\mathrm{K}}^{\mathrm{e}} \sim 57\%$ for photons and electrons, respectively. The less-efficient heralding of photons follows from considerably higher losses in their output coupling and detection [see (*27*) S1.4]. Not being a fundamental physical limitation, we expect appreciable improvements on the photon collection efficiency with technical optimizations, including use of superconducting detectors and strongly overcoupled resonators. Taking into account particle losses in transmission and detection, we estimate intrinsic heralding efficiencies η_{I}^{i} of ~50%. In principle, near-unity intrinsic heralding efficiencies can be achieved (*21*) [see detailed estimate of η_{I}^{i} in (*27*) S2.3].

Employing both particle channels facilitates correlation-enhanced measurements, isolating physical scattering events from uncorrelated noise such as detector dark counts. As a figure of merit for noise suppression, the fraction of true coincidences $R_{\mathrm{pe}}/(R_{\mathrm{pe}} - R_{\mathrm{acc}})$, with the uncorrelated (accidental) background rate R_{acc}, is defined for selecting a specific time-delay and energy-loss window (Fig. 3D), reaching 98.6%—i.e., a coincidence-to-accidental ratio (CAR) of ~75 [see (*27*) S1.6]. This demonstrates the high-fidelity generation of correlated electron-photon pairs, promising quantum-enhanced imaging.

Here we provide a proof-of-concept demonstration of coincidence-gated raster mapping of the resonator mode. Specifically, Fig. 4, A and B, shows the time-integrated electron and photon signals, respectively, and Fig. 4C displays the correlated events only. To quantify the correlation-induced improvement in image contrast, Fig. 4D compares the respective count rates for the individual and correlated signals on a logarithmic scale. Both the photon and electron signals trace the exponential decay of the evanescent field away from the structure, leveling off at constant values for larger distances. These background offsets limit the dynamic range of the mode imaging and are determined by the uncorrelated noise rates—i.e., the photodetector dark counts (130 counts/s) and residual overlap of the ZLP with the energetic gate (1.5×10^4 counts/s), respectively. Rejecting the uncorrelated background, the correlated signal (Fig. 4D, yellow curve) resolves the evanescent decay of the cavity field over longer distances. Despite a slightly smaller signal ($\eta_{\mathrm{K}}^{e} < 1$), we improve the dynamic range by two orders of magnitude [see (*27*) S2.5].

From a broader perspective, harnessing correlations of electrons with radiative emission (*34*) shows promise for enhancing contrast and resolution, as recently shown in the study of

core-level (*35*) and valence electronic excitations in nanostructured materials (*36*). Using postselection in the electronic and photonic degrees of freedom (*9*, *13*), such schemes can be generalized to trace state-specific scattering cross sections and create heralded pair states as a function of linear or angular momentum, polarization or spin, or frequency or energy.

Our findings demonstrate and apply the parametric generation of electron-photon pair states. Besides showing the capability for contrast enhancement in correlation-gated imaging, we implement flexible on-chip electron-heralded photon and photon-heralded single-electron sources. The integrated photonics platform allows for flexible electron-light phase-matching and spectral tuning of the generated cavity state. Postselection of multiloss electron events will facilitate a unique approach to generate tailored and higher-order photon Fock states. By merging free-electron quantum optics with integrated photonics, we provide a pathway toward a new class of hybrid quantum technology that relies on entangled electrons and photons, with applications ranging from photonic quantum state synthesis to quantum-enhanced sensing and imaging.

REFERENCES AND NOTES

1. P. G. Kwiat *et al*., *Phys. Rev. Lett.* **75**, 4337–4341 (1995).
2. N. Gisin, R. Thew, *Nat. Photonics* **1**, 165–171 (2007).
3. F. Borselli *et al*., *Phys. Rev. Lett.* **126**, 083603 (2021).
4. B. Hensen *et al*., *Nature* **526**, 682–686 (2015).
5. R. Riedinger *et al*., *Nature* **556**, 473–477 (2018).
6. P. Kruit *et al*., *Ultramicroscopy* **164**, 31–45 (2016).
7. A. E. Turner, C. W. Johnson, P. Kruit, B. J. McMorran, *Phys. Rev. Lett.* **127**, 110401 (2021).
8. V. Di Giulio, M. Kociak, F. J. G. de Abajo, *Optica* **6**, 1524 (2019).
9. E. Rotunno *et al*., arXiv:2106.08955 [quant-ph] (2021).
10. M. Tsarev, A. Ryabov, P. Baum, *Phys. Rev. Lett.* **127**, 165501 (2021).
11. Y. Pan, A. Gover, *Phys. Rev. A* **99**, 052107 (2019).
12. Z. Zhao, X.-Q. Sun, S. Fan, *Phys. Rev. Lett.* **126**, 233402 (2021).
13. A. Ben Hayun *et al*., *Sci. Adv.* **7**, eabe4270 (2021).
14. O. Kfir, V. Di Giulio, F. J. G. de Abajo, C. Ropers, *Sci. Adv.* **7**, eabf6380 (2021).
15. A. Polman, M. Kociak, F. J. García de Abajo, *Nat. Mater.* **18**, 1158–1171 (2019).
16. J. Christopher *et al*., *Nanophotonics* **9**, 4381–4406 (2020).
17. C. Roques-Carmes *et al*., *Science* **375**, eabm9293 (2022).
18. R. Bourrellier *et al*., *Nano Lett.* **16**, 4317–4321 (2016).
19. S. Meuret *et al*., *Phys. Rev. Lett.* **114**, 197401 (2015).
20. M. Solà-Garcia *et al*., *ACS Photonics* **8**, 916–925 (2021).
21. X. Bendaña, A. Polman, F. J. García de Abajo, *Nano Lett.* **11**, 5099–5103 (2011).
22. N. Müller *et al*., *ACS Photonics* **8**, 1569–1575 (2021).
23. Y. Auad *et al*., *Nano Lett.* **22**, 319–327 (2022).
24. M. Scheucher, T. Schachinger, T. Spielauer, M. Stöger-Pollach, P. Haslinger, arXiv:2110.05126 [physics.optics] (2021).
25. O. Kfir, *Phys. Rev. Lett.* **123**, 103602 (2019).
26. J.-W. Henke *et al*., *Nature* **600**, 653–658 (2021).
27. Materials and methods are available as supplementary materials.
28. M. H. P. Pfeiffer *et al*., *Optica* **3**, 20 (2016).
29. M. Kozák *et al*., *Opt. Express* **25**, 19195–19204 (2017).
30. N. V. Sapra *et al*., *Science* **367**, 79–83 (2020).
31. R. Dahan *et al*., *Science* **373**, eabj7128 (2021).
32. O. Kfir *et al*., *Nature* **582**, 46–49 (2020).
33. N. Talebi, *New J. Phys.* **16**, 053021 (2014).
34. R. J. Graham, J. Spence, H. Alexander, *Proc. MRS* **82**, 235 (1986).
35. D. Jannis, K. Müller-Caspary, A. Béché, J. Verbeeck, *Appl. Sci.* **11**, 9058 (2021).
36. N. Varkentina *et al*., arXiv:2202.12520 [cond-mat.mes-hall] (2022).
37. A. Feist *et al*., Figure data for cavity-mediated electron-photon pairs, version 1, Zenodo (2022); https://doi.org/10.5281/zenodo.6639005.

ACKNOWLEDGMENTS

We thank R. Haindl and E. Maddox for discussions on electron event clustering, M. Möller for supporting the scanning transmission electron microscope alignment, and J. Borchert and T. Weitz for providing us with the near-infrared spectrometer. We thank members of the eBEAM consortium—in particular A. Polman, F. J. García de Abajo, N. Talebi, J. Verbeeck, and M. Kociak—for useful discussions and feedback. **Funding:** All samples were fabricated in the Center of MicroNanoTechnology (CMi) at EPFL. This material is based on work supported by the Air Force Office of Scientific Research under award FA9550-19-1-0250. This work was further supported by the Swiss National Science Foundation under grant agreement 185870 (Ambizione). The experiments were conducted at the Göttingen UTEM Lab, funded by the Deutsche Forschungsgemeinschaft (DFG; German Research Foundation) through 432680300/SFB 1456 (project C01) and the Gottfried Wilhelm Leibniz program, and the European Union's Horizon 2020 (EU H2020) research and innovation programme under grant agreement 101017720 (FET-Proactive EBEAM). Y.Y. acknowledges support from the EU H2020 research and innovation program under the Marie Skłodowska-Curie IF grant agreement 101033593 (SEPhIM). O.K. acknowledges the Max Planck Society for funding from the Manfred Eigen Fellowship for postdoctoral fellows from abroad. **Author contributions:** Conceptualization: C.R., O.K., and T.J.K. Methodology: A.F. and G.A. (event-based spectroscopy), A.S.R., O.K., and J.L. (sample design), and G.H. and C.R. (theory). Investigation: A.F., G.A., J.-W.H., and F.J.K. (transmission electron microscopy experiments and optical setup), Y.Y. and G.H. (numerical simulation), and A.S.R. and Y.Y. (sample packaging and characterization). Formal analysis: A.F., G.A., G.H., and H.L.-M. Resources: J.L., Z.Q., and R.N.W. (sample fabrication). Project administration, supervision, and funding acquisition: C.R. and T.J.K. Visualization: A.F., G.H., G.A., and Y.Y. Writing: A.F., G.H., G.A., Y.Y., T.J.K., and C.R., with comments and feedback from all authors. **Competing interests:** The authors declare no competing interests. **Data and materials availability:** The code and data used to produce the plots within this work are available in Zenodo (*37*).

SUPPLEMENTARY MATERIALS

science.org/doi/10.1126/science.abo5037
Materials and Methods
Supplementary Text
Figs. S1 to S9
Table S1
References (*38*–*80*)

Submitted 25 February 2022; accepted 7 July 2022
10.1126/science.abo5037

Cavity-mediated electron-photon pairs

Armin FeistGuanhao HuangGermaine ArendYujia YangJan-Wilke HenkeArslan Sajid RajaF. Jasmin KappertRui Ning WangHugo Lourenço-MartinsZheru QiuJunqiu LiuOfer KfirTobias J. KippenbergClaus Ropers

Science, 377 (6607), • DOI: 10.1126/science.abo5037

Generating electron-photon pairs

The interaction of electron beams with cavities and resonant structures represents a universal scheme for generating electromagnetic radiation. Feist *et al*. fabricated structures with phase-matched interactions between free electrons and the vacuum cavity field of a photonic chip-based microresonator. As the electrons passed near the resonator, coupling between them and the vacuum field resulted in the spontaneous generation of photons within the cavity. Because the electron-photon pairs are correlated, they should be a useful source for the development of free-electron quantum optics providing enhanced imaging and sensing capabilities. —ISO